# Interface Morphogenesis with a Deformable Secondary Phase in Solid-State Lithium Batteries

**Authors:** Sun Geun Yoon[1], Bairav S. Vishnugopi[2], Douglas Lars Nelson[3], Adrian Xiao Bin Yong[4,5], Yingjin Wang[6], Stephanie Elizabeth Sandoval[1,3], Talia A. Thomas[1], Kelsey Anne Cavallaro[3], Pavel Shevchenko[7], Elif Pınar Alsaç[1], Congcheng Wang[1], Aditya Singla[2], Julia R. Greer[6], Elif Ertekin[5,8], Partha P. Mukherjee[2], Matthew T. McDowell[1,3]*

**Affiliations:**

1 George W. Woodruff School of Mechanical Engineering, Georgia Institute of Technology, Atlanta, Georgia, USA

2 School of Mechanical Engineering, Purdue University, West Lafayette, Indiana, USA

3 School of Materials Science and Engineering, Georgia Institute of Technology, Atlanta, Georgia, USA

4 Department of Materials Science and Engineering, University of Illinois Urbana-Champaign, Urbana, Illinois, USA

5 Materials Research Laboratory, University of Illinois Urbana-Champaign, Urbana, Illinois, USA

6 Division of Engineering and Applied Sciences, California Institute of Technology, Pasadena, California, USA

7 Advanced Photon Source, Argonne National Laboratory, Lemont, IL, USA

8 Department of Mechanical Science and Engineering, University of Illinois Urbana-Champaign, Urbana, Illinois, USA


*Corresponding Author: mattmcdowell@gatech.edu

**Abstract:** The complex and uncontrolled morphological evolution of lithium metal at the interface with solid-state electrolytes limits performance of solid-state batteries, leading to inhomogeneous reactions and contact loss. Inspired by biological morphogenesis, we introduce a new interfacial self-regulation concept in which a deformable secondary phase dynamically aggregates at the interface in response to local electro-chemo-mechanical stimuli, serving to enhance contact. Stripping of a lithium electrode containing 5-20% redox-inactive sodium domains causes spontaneous sodium accumulation across the interface, with the sodium undergoing local plastic deformation as lithium is removed to attain intimate electrical contact without blocking transport channels. This process, characterized with *operando* X-ray tomography and electron microscopy, mitigates void formation and substantially improves battery cycling performance at the low stack pressures needed for practical applications. The counterintuitive strategy of adding inactive alkali metal to improve performance demonstrates that interfacial self-regulation is a promising pathway to efficient solid-state batteries.

**Main Text:**

**Introduction**

  The high specific capacity of lithium metal and its compatibility with various solid-state electrolytes (SSEs) has focused efforts on developing lithium metal solid-state batteries (SSBs) *(1-4)*. However, a critical limitation of lithium metal anodes for SSBs is the loss of contact at the SSE interface during lithium stripping (*i.e.*, battery discharge) due to void formation *(1,2,5,6)*. The formation of voids is detrimental because they cause high interfacial impedance and current focusing during charging, resulting in lithium filament growth, short circuiting, and cell failure *(7-10)*.

  The mechanisms governing void formation are complex, and the process is affected by current density, stack pressure, chemo-mechanics, and other factors *(7,9,11-15)*. During stripping, vacancies are formed in the lithium metal at the SSE interface due to Li$^+$ transfer into the SSE. Since lithium metal exhibits relatively low self-diffusivity ($\sim 10^{-10}$ cm$^2$ s$^{-1}$) *(16-19)*, the vacancies tend to accumulate to nucleate voids (Fig. 1a). Higher current densities increase the vacancy formation rate and can thus accelerate void formation *(9,13,16,20)*. The application of stack pressure can deform soft lithium metal (bulk yield strength of 0.8 MPa) to promote contact retention during stripping, but stack pressures greatly exceeding the yield strength have been shown to be required at moderate current densities to prevent void formation (>7 MPa for 1 mA cm$^{-2}$) *(7,9)*. Moreover, lithium shows heightened yield strength at sub-micron length scales, which may result in even higher stack pressures needed when using SSE interfaces with nanoscale roughness *(21-24)*. Critically, stack pressures must be less than ~1 MPa for practical applications *(25-27)*. These factors urgently motivate the development of lithium anodes that retain interfacial contact at high current densities and low stack pressures.

  A variety of interfacial engineering approaches has been pursued to improve the performance of lithium metal anodes in SSBs. Interlayers comprising other materials, such as carbon or lithium metal alloys, have been shown to enable improved performance. In general, these interlayer or composite materials enhance Li transport toward the SSE interface, homogenize current distributions, and can help maintain interfacial contact *(28-32)*. However, these approaches have primarily utilized hard or brittle interlayer materials to passively control Li transport, and some of these materials undergo transformations themselves *(33-35)*. These approaches therefore usually require stack pressures similar to that needed for Li metal to maintain interfacial contact (see Fig. S1). New interfacial strategies are needed that feature materials that can dynamically respond to local driving forces to promote contact retention even at low stack pressures.

  Here, we introduce a new approach to regulate SSB interfaces that is inspired by biological morphogenesis, which is the process by which living cells self-organize to form patterns and structures via multi-length scale chemo-mechanical interactions *(36)*. Our approach involves self-regulated accumulation

of a secondary phase at the SSE interface in response to the evolving morphological irregularities caused by lithium stripping, thereby sustaining interfacial contact and improving behavior at low stack pressures. The approach is demonstrated using Li electrodes containing distributed metallic Na domains at relatively low concentrations (<20% Na). Na is electrochemically inactive, electrically conductive, and mechanically softer than lithium (the bulk yield strength of sodium is 0.16-0.24 MPa, Table S2). The Na dynamically accumulates at the interface during Li stripping and plastically deforms to create intimate electrical contact (Fig. 1b), which suppresses void formation and enhances stripping capacity at stack pressures <1 MPa without blocking Li. The accumulation and deformation of the Na enables morphogenic self-regulation at the Li-SSE interface, with Na contact spontaneously emerging without external guidance in response to electrochemical and mechanical stimuli *(36,37)*. The electrical conductivity of Na facilitates subsequent uniform Li plating, avoiding current constrictions and enabling stable cycling at low stack pressures. This strategy demonstrates the benefits of interface self-regulation through electrode microstructure control, potentially accelerating progress toward practical SSBs.

**Electrochemical stripping and plating**

Li/Na foils containing between 2.5 and 20 mol % Na were fabricated using accumulative roll bonding (see Methods). Figure S2 displays cross-sectional cryogenic focused-ion beam (FIB) scanning electron microscopy (SEM) images of the binary metals, showing distinct Na domains a few to ten micrometers in size surrounded by a continuous Li matrix. Na and Li are immiscible at room temperature, giving rise to the two-phase microstructure *(38)*. The standard electrode potential of Na is greater than Li (-2.71 and -3.04 vs. SHE, respectively, see Table S2), suggesting that Na should remain metallic and electrochemically inactive during Li redox processes *(39)*.

Figure 1c shows voltage curves during electrochemical stripping of Li from various Li/Na electrodes at stack pressures between 0 and 3.2 MPa. Solid-state half cells were used with argyrodite $Li_6PS_5Cl$ SSE (LPSC). Pure Li showed almost 30 mAh cm$^{-2}$ stripping capacity up to 0.5 V cutoff at 3.2 MPa stack pressure, but significantly less lithium was accessible at lower stack pressures (2.2 mAh cm$^{-2}$ at 0.8 MPa and 0.4 mAh cm$^{-2}$ at 0 MPa). This is a result of uncompensated void formation during stripping at low stack pressure *(28,29,40)*. The stripped capacities of the Li/Na electrodes were generally higher than pure Li at stack pressures below 1.6 MPa. For example, the 5% Na electrode delivered 16 mAh cm$^{-2}$ at 0.8 MPa stack pressure and the 20% Na electrode was able to strip 5.3 mAh cm$^{-2}$ at zero stack pressure. The voltage profiles of the electrodes in Fig. 1c show voltage variations at 0.15-0.25 V (also see the differential capacity curves in Fig. S3) which were absent during stripping of pure Li electrodes. This behavior likely arises from some interfacial oxidation of the Na since the potential is near the Na electrode potential.

Figure 1d shows statistical trends of the average stripped Li capacities for the different electrodes at varying stack pressure. While the pure Li and 2.5% Na electrodes showed monotonically increasing

capacity with increasing stack pressure, the other composite electrodes showed similar capacities at stack pressures between 0.8 and 3.2 MPa. The electrode with 20% Na is a limiting example, showing approximately invariant stripped capacity regardless of stack pressure, with lower stripped capacities at higher stack pressures that may arise from early blocking of Li transport to the interface.

A comprehensive summary of the initial stripping behavior of these electrodes at various current densities and stack pressures is shown in the maps in Fig. 1e. The color of the points represents the voltage either after 3.0 mAh cm$^{-2}$ was stripped or at the cutoff voltage of 0.62 V if this capacity was not reached (see Fig. S4a). The pure Li electrode can only strip this capacity at stack pressures >3.2 MPa. In contrast, the mixed electrodes with 5 and 10% Na allowed for successful stripping with <0.1 V at stack pressures down to 0.8 MPa and varying current densities. The stable stripping region for the 20% Na electrode was limited to lower current densities than composites with less Na. Further experiments were carried out to compare stripping from the various electrodes at zero applied stack pressure (Fig. S5 and Supplementary Text 1). Data at different current densities were fit to Sand's equation to extract an interfacial transport descriptor *(28,29,40)*, revealing that increasing Na content in the electrodes systematically enhances the effective transport of Li to the SSE interface. This implies that the incorporated Na phase stabilizes interfacial contact at zero stack pressure.

Electrochemical behavior during further plating and stripping cycles was also investigated (Fig. S4). After initial stripping, 3 mAh cm$^{-2}$ of Li was redeposited onto the working electrodes, followed by a second stripping process. Pure Li electrodes short circuited under all current density/stack pressure conditions during redeposition. Many of the Li/Na electrodes, and particularly those with 5 and 10% Na, did not short circuit upon plating (Fig. S4). During the second stripping process, the composite electrodes tended to exhibit higher polarization than the first, but stable stripping to 3 mAh cm$^{-2}$ was achieved for the composite electrodes across a range of current densities and stack pressures. Electrodes with 10% and 20% Na showed the lowest voltage at 0.8 MPa stack pressure during the second stripping. These results therefore show that the Na composites not only enable stable electrodeposition after the initial stripping step, but the presence of Na also beneficially influences the second stripping process.

**Interfacial evolution**

To provide insight into interfacial evolution, potentiostatic electrochemical impedance spectroscopy (EIS) was conducted during Li stripping. Figure 2a-b show galvanostatic stripping curves and Nyquist plots collected at increments of 0.5 mAh cm$^{-2}$ capacity from pure Li and 10% Na electrodes at 1.6 MPa stack pressure. The spectral features at high frequency (~1 MHz) likely arise from bulk SSE resistance, while lower frequency (100-1 kHz) features are associated with interfacial resistance, including interphase and charge transfer resistance *(7,31,32,41,42)*. At the onset of stripping, the voltages of the pure Li cell

https://doi.org/10.26434/chemrxiv-2025-xdzgq ORCID: https://orcid.org/0000-0001-5552-3456 Content not peer-reviewed by ChemRxiv. License: CC BY-NC 4.0

(Fig. 2a) and the 10% Na cell (Fig. 2b) were both 11 mV. The initial EIS spectra of both cells were also quite similar, showing compact spectra with minima at 36-38 $\Omega\,cm^2$. After stripping of the pure Li electrode to 5 mAh cm$^{-2}$, the cell voltage increased to 63 mV and a semicircle grew in the impedance spectra to a width of ~200 $\Omega\,cm^2$ (Fig. 2a). The apex frequency of this semicircle shifted to lower values during stripping (Fig. S6a), indicating that this feature is associated with voids at the interface that cause loss of contact (32,43,44). In contrast, the impedance spectrum of the 10% Na cell (Fig. 2b) showed no semicircle and only a minor shift of the spectrum to ~41 $\Omega\,cm^2$ during stripping, which was accompanied by a smaller voltage increase to 41 mV in the galvanostatic data. Notably, these EIS spectra showed the formation of a straight low-frequency tail (<1 kHz), which was also observed in Li/Na electrodes with other compositions (Fig. S7). Higher Na concentrations typically led to earlier tail development and higher voltages in the galvanostatic profiles at the end of stripping (Figs. S6b, c and S7).

The evolution of the EIS spectra from the Li-Na cells allows for the following conclusions. The lack of semicircle formation indicates that the electrode/SSE interface retains low resistance with minimal void formation during stripping, and the growth of the low-frequency tails is likely due to accumulation of the ion-blocking Na phase at the interface (45,46) (Fig. S8 contains control experiments with Na/Na symmetric cells demonstrating blocking behavior). This result implies that excessive Na content (20% Na and above) causes faster voltage polarization because of the more rapid accumulation of Na at the interface to block Li transport, rather than through void formation.

The morphological evolution of the interface was investigated with cryo-FIB-SEM (Fig. 2e, f). In the initial state, a 10% Na electrode (Fig. 2e, Fig. S9a) shows micron-scale Na domains distributed uniformly throughout the darker Li, without contact between Na and the SSE material. After stripping 4 mAh cm$^{-2}$ in a different cell (Fig. 2f), the electrode showed a few-micron thick Na layer that seamlessly contacted the SSE. This behavior is due to accumulation of Na at the interface during Li stripping, with the Na maintaining electrical contact (Fig. 2b).

The reversibility of this behavior was investigated to understand how the accumulated Na interfacial layer evolves upon subsequent Li plating. As displayed in the galvanostatic data in Fig. 2c, stable Li deposition occurs without nucleation overpotential after the first stripping. Figure 2g contains a cryo-FIB-SEM image that shows that the accumulated Na layer moves away from the interface as Li is deposited onto it. After the first cycle, the second and third stripping steps showed similar EIS evolution and final voltage values as the first stripping step (Fig. 2c, d). The low-frequency EIS tails appear during the second and third stripping steps similarly to the first step. This is consistent with a cryo-FIB-SEM image in Fig. S9d, showing interfacial Na accumulation after partial stripping even after multiple cycles. Overall, these results indicate that Na returns to contact the SSE interface during cyclic Li stripping without substantial void formation. Moreover, the EIS signatures suggest that Na accumulates at the interface even before the deposited Li layer is fully depleted (Fig. S9d).

5

**Operando X-ray computed tomography**

The dynamic evolution of a Li/Na electrode was investigated using *operando* synchrotron X-ray computed tomography (XCT) imaging. A half cell with a 10% Na electrode was used in a cell customized for XCT imaging during electrochemical testing (see Methods). Fig. 3a shows a cross-sectional image slice of the cell stack. The grayscale contrast between both electrodes and LPSC is due to differences of the X-ray attenuation coefficients of each material *(10,47)*, with the electrodes appearing darker since they are primarily composed of low-Z Li metal *(10,48,49)*.

Galvanostatic stripping and plating were performed sequentially using a current density of 0.5 mA cm$^{-2}$, with stripping and plating capacities of 1.0 and 1.13 mAh cm$^{-2}$, respectively (Fig. S10). Magnified image slices of a location at the interface between the SSE and the Li/Na electrode at various times are shown in Fig. 3b. The bright domains in the electrode are Na. To highlight the evolution of Na at the interface, grayscale intensity profiles across the interface are displayed below the image slices in Fig. 3b, with scanned locations indicated by red boxes in the images. The boundary between the electrode and SSE is marked with a red line in each intensity plot. As shown in the profile in Fig. 3b(i), the composite electrode exhibits greater intensity variation compared to the SSE region. Grayscale intensity peaks and valleys in the electrode correspond to the Na domains and the Li matrix, respectively. The average grayscale pixel intensity values of the electrode and the SSE regions in this profile are 98.1 ± 65.2 and 124.3 ± 22.9, respectively, consistent with other locations (Fig. S11 and Supplementary Text 3).

During electrochemical cycling, three different Na domains were tracked in the electrode, with the peaks associated with these domains marked with green and blue lines in the intensity profiles in Fig. 3b. The first Na domain closest to the SSE interface (green line) initially remained separated from the SSE interface (red line) by a Li layer (Fig. 3b(i)). During Li stripping, this Na peak moved closer and became conflated with the SSE interface (Fig. 3b(ii-iv)). During Li plating, the Na peak again became distinct from the SSE as Li deposited below it (Fig. 3b(iv-vi)). This behavior is consistent with the *ex-situ* SEM in Fig. 2g and demonstrates the accumulation and removal of Na from the interface. The other Na peaks in the intensity trace were also displaced during cycling as Li was stripped and re-deposited at the electrode (blue lines in Fig. 3b). This Na domain movement during stripping and plating was consistent with analysis of a different location (Fig. S11).

As discussed in Fig. 2, the Li/Na electrode exhibits a different interfacial distribution of Na after one cycle compared to its initial state. To understand how the accumulation of Na at the interface depends on the initial distribution of Na within the microstructure, we developed an analysis procedure to simulate Li stripping using the 3D XCT data. This "simulated stripping" analysis was carried out instead of direct segmentation of Na at the interface since the Na and the SSE phases exhibited similar grayscale intensity (Fig. 3b), which precluded accurate segmentation of these phases when in contact. The reconstructed

6

microstructure of the pristine composite electrode is shown in Fig. 3c. The simulated stripping process involved virtually "removing" a planar layer of Li voxels and projecting the Na voxels in the same layer onto the SSE interface, followed by identical processing of the next layers (Fig. S12). Figure 3d displays the evolution of interfacial coverage of Li and Na as a function of stripped Li thickness up to 14 μm (10 voxel layers, equivalent to 2.9 mAh cm$^{-2}$). Stripping was simulated for both the pristine XCT microstructure (i.e., Fig. 3b(i)) and the microstructure after one cycle (i.e., Fig. 3b(vi)). The corresponding 2D maps of Li and Na coverage across a region of the interface are shown in Fig. 3e. As shown in Fig. 3d, e(i-iii), the interfacial coverage of Na during the first stripping increased steadily as Li was stripped and its coverage decreased. During the second stripping, however, a non-linear and more abrupt increase of Na coverage was observed (Fig 3d, e(iv-vi)). This more abrupt increase during the second stripping is due to the Li layer beneath the accumulated Na being depleted to result in sudden Na/SSE contact. Thus, the microstructural distribution of Na in the composite is expected to strongly influence Na contact pattern formation at the interface and resulting electrochemical behavior.

**Electrochemical cycling**

Galvanostatic cycling tests were carried out to investigate electrochemical reversibility. Cells with LiIn counter electrodes were cycled with 2 mAh cm$^{-2}$ capacity per cycle. As shown in Fig. 4a, all the Li/Na electrodes with different compositions showed reversible cycling over 10 cycles. Figure 4b(i-iv) presents the overlaid stripping voltage profiles over four cycles. The voltage profiles during the first stripping generally exhibited a linear increase, with their slopes being approximately proportional to Na concentration. Following the first stripping cycle, subsequent stripping profiles showed nonlinear increases, especially with higher Na concentrations. These features indicate that the Na distribution affects the extent of voltage polarization, as the more abrupt accumulation of the Na phase at the SSE interface observed in the second cycle in the XCT data in Fig. 3d gives rise to more rapid polarization. The 5% and 10% Na electrodes also exhibited stable cycling upon doubling the cycling capacity to 4 mAh cm$^{-2}$ per cycle (Fig. S13).

Longer-term galvanostatic cycling tests were also conducted. Figure 4c, d show cycling results for a 5% Na electrode at a current density of 0.75 mA cm$^{-2}$ and a stack pressure of 2.5 MPa (Fig. 4c) and a 10% Na electrode at a current density of 0.5 mA cm$^{-2}$ and a stack pressure of 1.6 MPa (Fig. 4d). Under these conditions, pure Li electrodes typically exhibited rapid voltage polarization during stripping due to voiding at the interface, followed by short circuiting during plating (insets in Fig. 4c, d). In contrast, the cells with Li/Na electrodes showed significantly enhanced cyclability and low voltage. The 5% Na electrode (Fig. 4c) and the 10% Na electrode (Fig. 4d) sustained over 100 and 50 cycles, respectively. Additionally, the 5% Na electrode demonstrated outstanding cyclability at a current density of 1 mA cm$^{-2}$ and a stack pressure

of 4.1 MPa (Fig. S14). These results demonstrate that the accumulation of Na at the SSE interface not only mitigates voiding, but due to its electrochemical inactivity and deformability it also supports stable Li plating (Fig. 2g), enabling cycling even at low stack pressures.

All-solid-state full cells with Li/Na anodes and sulfur composite cathodes were fabricated and tested under low stack pressures between 2.5 and 0.8 MPa (Figs. S15 and S16; Supplementary Text 4), which is much lower than most literature demonstrations of sulfur SSBs *(50,51)*. A cell with a 5% Na anode displayed >3 mAh cm$^{-2}$ and 75% capacity retention after 100 cycles with 2.5 MPa stack pressure (Fig. S15), whereas cells with pure Li anodes short circuited in ~5 cycles. A cell with a 10% Na anode exhibited 69 cycles at a stack pressure of 0.8 MPa (Fig. S16a), whereas a pure Li cell short circuited in the first cycle. Overall, the Li/Na anode shows lower polarization and better interfacial contact than pure Li.

Figure S1 compares the experimental conditions (stack pressures and current density) from the results herein with other published SSBs demonstrations using Li metal and Li alloy electrodes with sulfide SSEs. Alloy anodes such as Si are frequently employed to overcome the challenges of Li metal, such as Li filament growth *(33-35)*. However, both Li metal and Li alloy anodes usually necessitate high stack pressures, ranging from a few MPa to several tens of MPa (Fig. S1). The literature survey shows that the required stack pressure generally rises with increased current density, with higher stack pressures needed to maintain the morphological conformity of the solid-solid interface *(35,52)*. Our multiphase alkali metal electrodes deviate from this trend, functioning effectively at stack pressures between 0.8 and 2 MPa with modest current densities (Fig. S16), highlighting a new interfacial self-regulation strategy for attaining operation under practical conditions.

**Electro-chemo-mechanical modeling**

A mesoscale model was developed to better understand how electro-chemo-mechanical interactions influence Na domain evolution at the SSE interface. The model considers electrochemical reaction kinetics, mechanical deformation of the metals, diffusivity, and ionic transport (see SI). Figure 5a illustrates the stress distribution in a pure Li electrode in the vicinity of a void at the Li-SSE interface (1 MPa stack pressure). The stresses diminish above the void due to the absence of contact between Li and the SSE, while stress concentration in the Li occurs near the void edges. Current focusing near the void edges during stripping leads to loss of contact at the Li-SSE interface and void growth (Fig. 5b, c). In contrast, a Na domain at the interface contacts both the SSE and Li, homogenizing the stress distribution with the Na domain under compressive stress (Fig. 5d). Since Na has a lower yield strength than Li (nanoindentation shows 54% lower hardness, Fig. S18) *(53-55)*, the stress exerted on the Na domain by the surrounding Li can induce plastic deformation and creep along the interface as Li is stripped. The simulation shows that this causes Na to deform and extend along the SSE interface as Li is removed (Fig. 5e, f), suppressing the formation of voids. From these results, we expect that it is the chemo-mechanical behavior

https://doi.org/10.26434/chemrxiv-2025-xdzgq ORCID: https://orcid.org/0000-0001-5552-3456 Content not peer-reviewed by ChemRxiv. License: CC BY-NC 4.0

of Na that enhances stripping behavior rather than a pure transport effect, as density functional theory calculations showed that Li-Na interfaces exhibit lower diffusivity than Li surfaces (Fig. S19 and Table S5).

The electric potential distributions within the SSE after 2 min of stripping for both simulated cases are shown in Fig. 5g, h for an applied current density $I_{App}$ = 0.5 mA cm$^{-2}$. The greater Li-SSE contact achieved with Na results in less current focusing at the interface (Fig. S20) and a more uniform potential distribution in the SSE domain. Fig. 5i, j shows the effect of void or Na domain size and applied current density on the Li-SSE contact evolution at $t$=2 min. The reaction heterogeneity at the interface increases and Li-SSE contact decreases with an increase in applied current density. An increase in void or Na domain size also exacerbates current heterogeneity due to the reduced Li-SSE interfacial contact. However, the action of Na in suppressing voids sustains higher interfacial contact fractions at higher current densities and domain sizes. The difference in Li-SSE contact evolution with and without Na is more pronounced for smaller voids due to the rapid growth of the void by Li surface diffusion. Figure 5k compares the reaction distribution for a void vs. Na domain with $I_{App}$ = 0.5 mA cm$^{-2}$ in the initial state ($t$=0 min) and after $t$=2 min. Initially, the interfacial contact region for the void and Na are the same, resulting in an identical reaction current distribution (Fig. 5k). As the interface evolves over time, more contact loss and current focusing occurs near the void compared to Na. Overall, these simulation results show that the deformability of Na promotes dynamic interfacial contact in response to local chemo-mechanical stimuli, suppressing void formation as Na accumulates at the interface.

## Conclusion

The morphological instabilities of the Li metal-SSE interface have long been a significant challenge for SSBs, and they have typically been addressed by applying unrealistically high pressures to the cell stack. Here, we demonstrate the concept of interfacial morphogenesis applied to lithium metal SSBs, in which interfacial properties are self-regulated across length scales in a multiphase electrode via global contact pattern formation and by local mechanical stimuli to promote interfacial contact. Binary Li/Na electrodes show the capability to suppress void growth through accumulation and deformation of the Na domains at the SSE interface, thereby enhancing Li stripping capacity at low stack pressures (<3.2 MPa). The inherently soft nature of the Na phase offers greater plastic deformability compared to the Li matrix, allowing it to effectively spread to contact the SSE interface as Li is removed. This behavior leads to Na accumulation and sustains electrical contact across the SSE interface, promoting subsequent uniform Li plating without current constriction and reversible cell cycling at stack pressures less than 1 MPa. Furthermore, the electrochemical inertness of the Na phase with respect to the active Li electrode enables it to repeatedly respond to morphological changes without undergoing electrochemical lithiation/delithiation, thus avoiding the structural degradation often seen in Li-reactive metal alloy or

9

carbon interlayers/composites *(31,35)*. Additionally, binary alkali metal foils can be created and cold-rolled with simple metallurgical techniques, avoiding more complex processing *(8,28-30,32)*. Overall, this study shows the promise of engineering lithium metal electrodes to include domains with tailored chemo-mechanical properties, which can accumulate at the interface during cycling to promote desired morphology evolution. Further development with other deformable materials with tailored electrochemical or mechanical properties is of interest.

## References

1. J. Janek, W. G. Zeier, Challenges in speeding up solid-state battery development. *Nat. Energy* **8**, 230-240 (2023). DOI: 10.1038/s41560-023-01208-9

2. K. B. Hatzell *et al.*, Challenges in lithium metal anodes for solid-state batteries. *ACS Energy Lett.* **5**, 922-934 (2020). DOI: 10.1021/acsenergylett.9b02668

3. K. J. Kim, M. Balaish, M. Wadaguchi, L. Kong, J. L. Rupp, Solid-state Li–metal batteries: challenges and horizons of oxide and sulfide solid electrolytes and their interfaces. *Adv. Energy Mater.* **11**, 2002689 (2021). DOI: 10.1002/aenm.202002689

4. B. S. Vishnugopi *et al.*, Challenges and opportunities for fast charging of solid-state lithium metal batteries. *ACS Energy Lett.* **6**, 3734-3749 (2021). DOI: 10.1021/acsenergylett.1c01352

5. T. Krauskopf, F. H. Richter, W. G. Zeier, J. Janek, Physicochemical concepts of the lithium metal anode in solid-state batteries. *Chem. Rev.* **120**, 7745-7794 (2020). DOI: 10.1021/acs.chemrev.0c00431

6. A. Banerjee, X. Wang, C. Fang, E. A. Wu, Y. S. Meng, Interfaces and interphases in all-solid-state batteries with inorganic solid electrolytes. *Chem. Rev.* **120**, 6878-6933 (2020). DOI: 10.1021/acs.chemrev.0c00101

7. J. Kasemchainan *et al.*, Critical stripping current leads to dendrite formation on plating in lithium anode solid electrolyte cells. *Nat. Mater.* **18**, 1105-1111 (2019). DOI: 10.1038/s41563-019-0438-9

8. V. Raj *et al.*, Direct correlation between void formation and lithium dendrite growth in solid-state electrolytes with interlayers. *Nat. Mater.* **21**, 1050-1056 (2022). DOI: 10.1038/s41563-022-01264-8

9. Y. Lu *et al.*, The void formation behaviors in working solid-state Li metal batteries. *Sci. Adv.* **8**, eadd0510 (2022). DOI: 10.1126/sciadv.add0510

10. J. A. Lewis *et al.*, Linking void and interphase evolution to electrochemistry in solid-state batteries using operando X-ray tomography. *Nat. Mater.* **20**, 503-510 (2021). DOI: 10.1038/s41563-020-00903-2

11.  M. J. Wang, R. Choudhury, J. Sakamoto, Characterizing the Li-solid-electrolyte interface dynamics as a function of stack pressure and current density. *Joule* **3**, 2165-2178 (2019). DOI: 10.1016/j.joule.2019.06.017

12.  X. Zhang, Q. J. Wang, K. L. Harrison, S. A. Roberts, S. J. Harris, Pressure-driven interface evolution in solid-state lithium metal batteries. *Cell Rep. Phys. Sci.* **1**, 100012 (2020). DOI: 10.1016/j.xcrp.2019.100012

13.  H. Yan *et al.*, How does the creep stress regulate void formation at the lithium-solid electrolyte interface during stripping? *Adv. Energy Mater.* **12**, 2102283 (2022). DOI: 10.1002/aenm.202102283

14.  B. S. Vishnugopi *et al.* Asymmetric Contact Loss Dynamics during Plating and Stripping in Solid-State Batteries. *Adv. Energy Mater.* **13**, 2203671 (2023). DOI: 10.1002/aenm.202203671

15.  A. Mistry, P. P. Mukherjee, Molar volume mismatch: a malefactor for irregular metallic electrodeposition with solid electrolytes. *J. Electrochem. Soc.* **167**, 082510 (2020). DOI: 10.1149/1945-7111/ab8ecd

16.  T. Krauskopf, H. Hartmann, W. G. Zeier, J. Janek, Toward a fundamental understanding of the lithium metal anode in solid-state batteries—an electrochemo-mechanical study on the garnet-type solid electrolyte $Li_{6.25}Al_{0.25}La_3Zr_2O_{12}$. *ACS Appl. Mater. Interfaces* **11**, 14463-14477 (2019). DOI: 10.1021/acsami.9b02537

17.  T. Jow, C. Liang, Interface between solid electrode and solid electrolyte—A study of the $Li/LiI(Al_2O_3)$ solid-electrolyte system. *J. Electrochem. Soc.* **130**, 737 (1983). DOI: 10.1149/1.2119795

18.  A. Lodding, J. Mundy, A. Ott, Isotope inter-diffusion and self-diffusion in solid lithium metal. *Phys. Status Solidi B* **38**, 559-569 (1970). DOI: 10.1002/pssb.19700380206

19.  E. Dologlou, Self-diffusion in solid lithium. *Glass Phys. Chem.* **36**, 570-574 (2010). DOI: 10.1134/S1087659610050056

20.  P. Barai *et al.*, Study of void formation at the lithium|solid electrolyte interface. *Chem. Mater.* **36**, 2245-2258 (2024).

21.  M. J. Wang, E. Kazyak, N. P. Dasgupta, J. Sakamoto, Transitioning solid-state batteries from lab to market: Linking electro-chemo-mechanics with practical considerations. *Joule* **5**, 1371-1390 (2021). DOI: 10.1016/j.joule.2021.04.001

22.  C. D. Fincher, D. Ojeda, Y. Zhang, G. M. Pharr, M. Pharr, Mechanical properties of metallic lithium: from nano to bulk scales. *Acta Mater.* **186**, 215-222 (2020). DOI: 10.1016/j.actamat.2019.12.036

23. C. Xu, Z. Ahmad, A. Aryanfar, V. Viswanathan, J. R. Greer, Enhanced strength and temperature dependence of mechanical properties of Li at small scales and its implications for Li metal anodes. *Proc. Natl. Acad. Sci. U.S.A.* **114**, 57-61 (2017). DOI: 10.1073/pnas.1615733114

24. M. A. Citrin *et al.*, From ion to atom to dendrite: Formation and nanomechanical behavior of electrodeposited lithium. *MRS Bull.* **45**, 891-904 (2020). DOI: 10.1557/mrs.2020.148

25. P. Albertus, *et al.* Challenges for and pathways toward Li-metal-based all-solid-state batteries. *ACS Energy Lett.* **6**, 1399-1404 (2021). DOI: 10.1021/acsenergylett.1c00445

26. J. Lee, T. Lee, K. Char, K. J. Kim, J. W. Choi, Issues and advances in scaling up sulfide-based all-solid-state batteries. *Acc. Chem. Res.* **54**, 3390-3402 (2021). DOI: 10.1021/acs.accounts.1c00333

27. T. Schmaltz *et al.*, A roadmap for solid-state batteries. *Adv. Energy Mater.* **13**, 2301886 (2023). DOI: 10.1002/aenm.202301886

28. T. Krauskopf, B. Mogwitz, C. Rosenbach, W. G. Zeier, J. Janek, Diffusion limitation of lithium metal and Li–Mg alloy anodes on LLZO type solid electrolytes as a function of temperature and pressure. *Adv. Energy Mater.* **9**, 1902568 (2019). DOI: 10.1002/aenm.201902568

29. T. Fuchs *et al.*, Increasing the pressure-free stripping capacity of the lithium metal anode in solid-state-batteries by carbon nanotubes. *Adv. Energy Mater.* **12**, 2201125 (2022). DOI: 10.1002/aenm.202201125

30. J. Aspinall *et al.*, The impact of magnesium content on lithium-magnesium alloy electrode performance with argyrodite solid electrolyte. *Nat. Commun.* **15**, 4511 (2024). DOI: 10.1038/s41467-024-48071-0

31. S. E. Sandoval *et al.*, Structural and electrochemical evolution of alloy interfacial layers in anode-free solid-state batteries. *Joule* **7**, 2054-2073 (2023). DOI: 10.1016/j.joule.2023.07.022

32. S. G. Yoon *et al.*, Synergistic evolution of alloy nanoparticles and carbon in solid-state lithium metal anode composites at low stack pressure. *ACS Nano* **18**, 20792-20805 (2024). DOI: 10.1021/acsnano.4c07687

33. J. A. Lewis, K. A. Cavallaro, Y. Liu, M. T. McDowell, The promise of alloy anodes for solid-state batteries. *Joule* **6**, 1418-1430 (2022). DOI: 10.1016/j.joule.2022.05.016

34. W. J. Jeong *et al.*, Electrochemical behavior of elemental alloy anodes in solid-state batteries. *ACS Energy Lett.* **9**, 2554-2563 (2024). DOI: 10.1021/acsenergylett.4c00915

35. S. Kim *et al.*, High-power hybrid solid-state lithium–metal batteries enabled by preferred directional lithium growth mechanism. *ACS Energy Lett.* **8**, 9-20 (2022). DOI: 10.1021/acsenergylett.2c02150

36. C. Collinet, T. Lecuit, Programmed and self-organized flow of information during morphogenesis. *Nat. Rev. Mol. Cell Biol.* **22**, 245-265 (2021). DOI: 10.1038/s41580-020-00318-6

37. R. Ramos *et al.*, Parsing patterns: Emerging roles of tissue self-organization in health and disease. *Cell* **187**, 3165-3186 (2024). DOI: 10.1016/j.cell.2024.05.016

38. C. Bale, The Li-Na (lithium-sodium) system. *Bull. Alloy Phase Diagrams* **10**, 265-268 (1989). DOI: 10.1007/BF02877509

39. S. Y. Kim, J. Li, Porous mixed ionic electronic conductor interlayers for solid-state batteries. *Energy Mater. Adv.* **2021**, 1519569 (2021). DOI: 10.34133/2021/1519569

40. Z.-X. Wang *et al.*, Suppressing Li voids in all-solid-state lithium metal batteries through Li diffusion regulation. *Joule* (2024). DOI: 10.1016/j.joule.2024.07.007

41. M. A. Kraft *et al.*, Influence of lattice polarizability on the ionic conductivity in the lithium superionic argyrodites $Li_6PS_5X$ (X= Cl, Br, I). *J. Am. Chem. Soc.* **139**, 10909-10918 (2017). DOI: 10.1021/jacs.7b06327

42. H. Huo *et al.*, Chemo-mechanical failure mechanisms of the silicon anode in solid-state batteries. *Nat. Mater.* **23**, 543-551 (2024). DOI: 10.1038/s41563-023-01792-x

43. J. K. Eckhardt *et al.*, Guidelines for impedance analysis of parent metal anodes in solid-state batteries and the role of current constriction at interface voids, heterogeneities, and SEI. *Adv. Mater. Interfaces* **10**, 2202354 (2023). DOI: 10.1002/admi.202202354

44. J. K. Eckhardt *et al.*, 3D impedance modeling of metal anodes in solid-state batteries– incompatibility of Pore Formation and constriction effect in physical-based 1D circuit models. *ACS Appl. Mater. Interfaces* **14**, 42757-42769 (2022). DOI: 10.1021/acsami.2c12991

45. J. Jamnik, J. Maier, S. Pejovnik, A powerful electrical network model for the impedance of mixed conductors. *Electrochim. Acta* **44**, 4139-4145 (1999). DOI: 10.1016/S0013-4686(99)00128-0

46. R. A. Huggins, Simple method to determine electronic and ionic components of the conductivity in mixed conductors a review. *Ionics* **8**, 300-313 (2002). DOI: 10.1007/BF02376083

47. P. Pietsch, V. Wood, X-ray tomography for lithium ion battery research: a practical guide. *Ann. Rev. Mater. Res.* **47**, 451-479 (2017). DOI: 10.1146/annurev-matsci-070616-123957

48. Z. Ning *et al.*, Visualizing plating-induced cracking in lithium-anode solid-electrolyte cells. *Nat. Mater.* **20**, 1121-1129 (2021). DOI: 10.1038/s41563-021-00967-8

49. D. Cao *et al.*, Nondestructively visualizing and understanding the mechano-electro-chemical origins of "soft short" and "creeping" in all-solid-state batteries. *Adv. Funct. Mater.* **33**, 2307998 (2023). DOI: 10.1002/adfm.202307998

50. J. Zhou *et al.*, Healable and conductive sulfur iodide for solid-state Li–S batteries. *Nature* **627**, 301-305 (2024). DOI: 10.1038/s41586-024-07101-z

51. S. Ohno, C. Rosenbach, G. F. Dewald, J. Janek, W. G. Zeier, Linking solid electrolyte degradation to charge carrier transport in the thiophosphate-based composite cathode toward solid-state lithium-sulfur batteries. *Adv. Funct. Mater.* **31**, 2010620 (2021). DOI: 10.1002/adfm.202010620

52. X. Hu *et al.*, External-pressure-electrochemistry coupling in solid-state lithium metal batteries. *Nat. Rev. Mater.* **9**, 305-320 (2024). DOI: 10.1038/s41578-024-00669-y

53. C. D. Fincher, Y. Zhang, G. M. Pharr, M. Pharr, Elastic and plastic characteristics of sodium metal. *ACS Appl. Energy Mater.* **3**, 1759-1767 (2020). DOI: 10.1021/acsaem.9b02225

54. M. J. Wang, J.-Y. Chang, J. B. Wolfenstine, J. Sakamoto, Analysis of elastic, plastic, and creep properties of sodium metal and implications for solid-state batteries. *Materialia* **12**, 100792 (2020). DOI: 10.1016/j.mtla.2020.100792

55. W. S. LePage, Y. Chen, A. Poli, M. Thouless, N. P. Dasgupta, Sodium mechanics: effects of temperature, strain rate, and grain rotation and implications for sodium metal batteries. *Extreme Mech. Lett.* **52**, 101644 (2022). DOI: 10.1016/j.eml.2022.101644
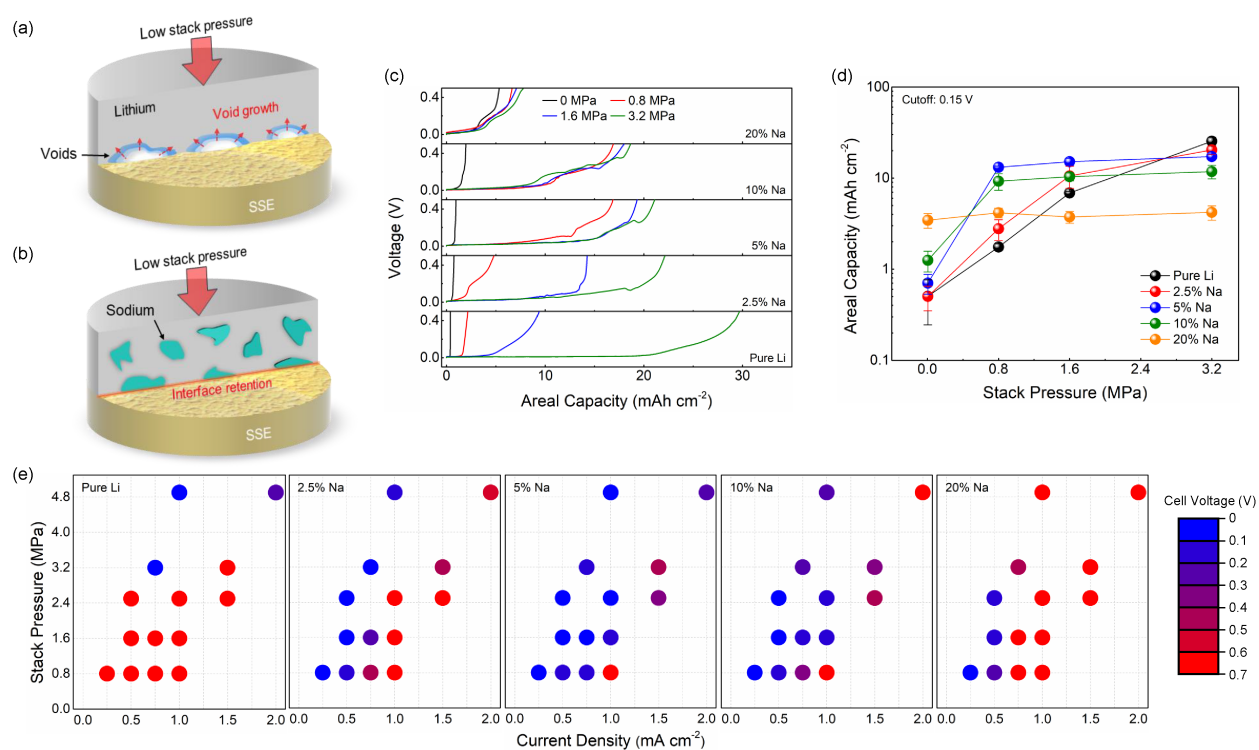
## Acknowledgments

**Figure 1. Electrochemical stripping and plating tests of Li/Na electrodes.** (a, b) Schematics of (a) void formation during pure Li stripping at low stack pressure, and (b) Na accumulation and void mitigation during stripping of a Li/Na electrode. (c) Galvanostatic voltage profiles during Li stripping from various Li/Na electrodes at different stack pressures. The cells used $Li_6PS_5Cl$ SSE, Li metal counter electrodes, and a current density of 0.25 mA $cm^{-2}$. (d) Average stripped areal capacity from different Li/Na electrodes (three experiments each) as a function of stack pressure. The stripped capacities were measured at a cutoff voltage of 0.15 V. Error bars represent standard deviation. (e) Color maps showing the cell voltage after 3 mAh $cm^{-2}$ of stripping or at a cutoff voltage of 0.62 V if this capacity was not reached, as a function of stack pressure (0.8 to 4.8 MPa, *y*-axis) and current density (0.25 to 2.0 mA $cm^{-2}$, *x*-axis). Working electrodes comprising pure Li, 2.5% Na, 5% Na, 10% Na, and 20% Na were used (left to right). A $Li_1In_3$ alloy (LiIn, +0.62 V *vs.* Li/Li$^+$) electrode was used as the counter electrode to avoid short circuiting. All percentages are molar percentages.
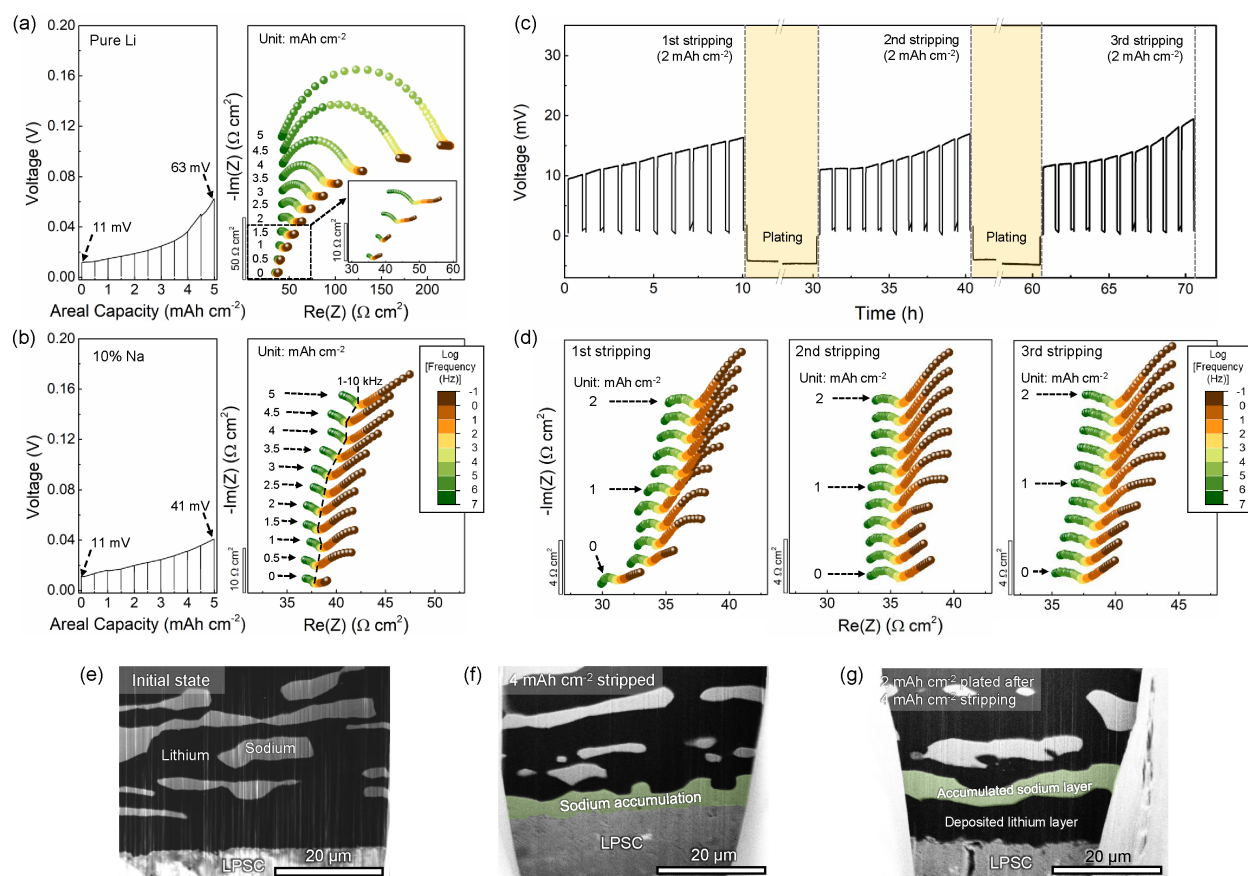
**Figure 2. Electrochemical impedance analysis of interfacial evolution.** (a, b) *In situ* EIS analysis of (a) the pure Li and (b) 10% Na electrodes during Li stripping with Li counter electrodes at 1.6 MPa stack pressure. The left panels display voltage profiles and the right panels display the associated Nyquist plots. A current density of 0.25 mA cm$^{-2}$ was used with potentiostatic EIS spectra taken every 0.5 mAh cm$^{-2}$, as marked. Impedance spectra for other compositions are shown in Fig. S7. (c, d) *In situ* EIS analysis of a 10% Na electrode during electrochemical cycling with a Li counter electrode at 2.5 MPa stack pressure. (c) Voltage profile and (d) associated Nyquist plots for the 1st, 2nd, and 3rd stripping steps. Current densities of 0.25 mA cm$^{-2}$ and 0.1 mA cm$^{-2}$ were used for stripping and plating, respectively. Potentiostatic EIS spectra were measured every 0.2 mAh cm$^{-2}$ during stripping, as marked. (e-g) Cryo-FIB-SEM images of 10% Na electrodes at various stages of cycling: (e) the initial state, (f) after 4 mAh cm$^{-2}$ was stripped, and (g) after 2 mAh cm$^{-2}$ was plated (following initial stripping of 4 mAh cm$^{-2}$). All cells in (e-g) had a stack pressure of 1.6 MPa and current density of 0.25 mA cm$^{-2}$. In (f) and (g), an artificial green color has been overlaid on interface-accumulated Na. Images without the overlays are shown in Fig. S9b, c.
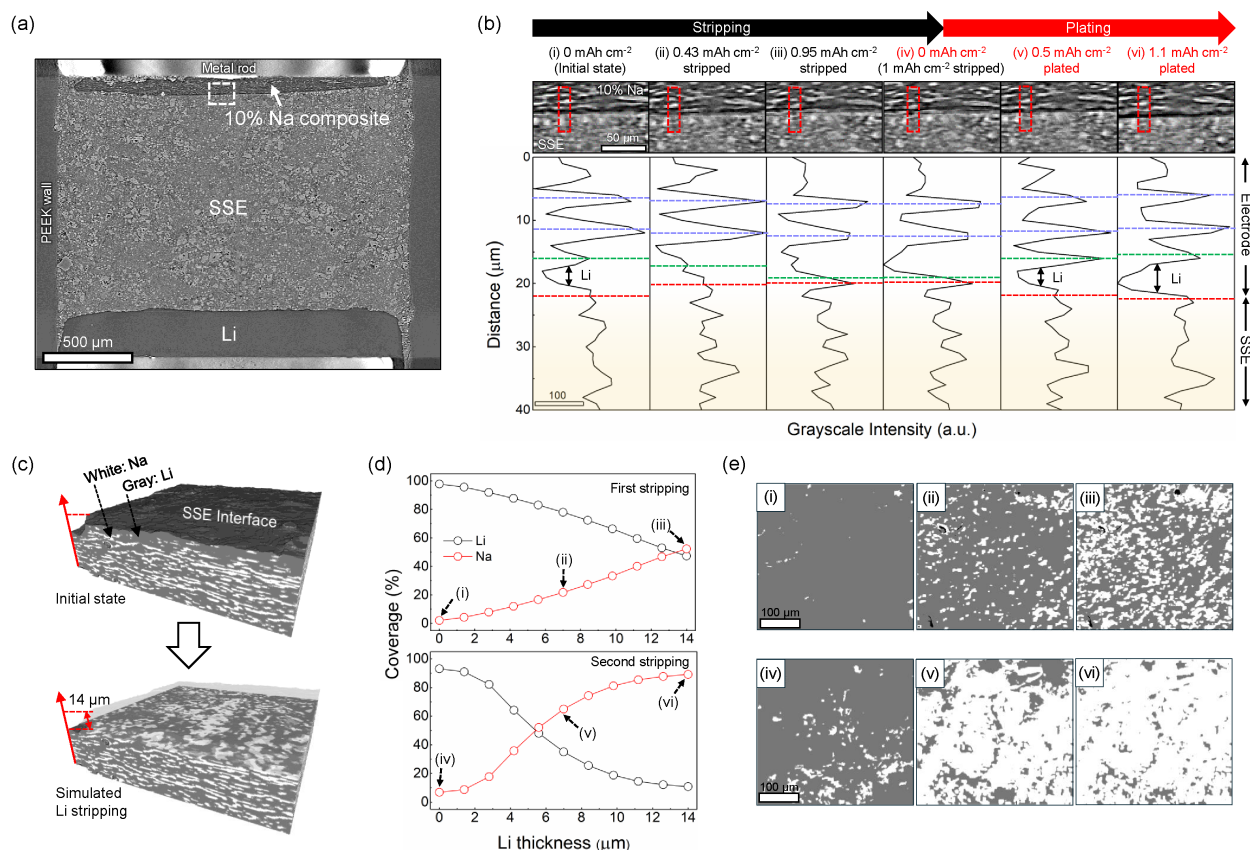
https://doi.org/10.26434/chemrxiv-2025-xdzgq **ORCID:** https://orcid.org/0000-0001-5552-3456 Content not peer-reviewed by ChemRxiv. **License:** CC BY-NC 4.0

**Figure 3. Operando X-ray CT analysis of interfacial evolution.** (a, b) *Operando* X-ray tomography imaging of a 10% Na composite electrode half cell during Li stripping and plating. (a) An image slice of the 10% Na electrode|LPSC|Li half cell. (b) Cross-sectional images of a portion of the interface between LPSC and the Li/Na electrode at different stages of cycling, along with corresponding grayscale intensity profiles from the red boxes in the images. The stages of electrochemical cycling are labeled from left to right as follows: (i) 0 mAh cm$^{-2}$ stripped (initial state), (ii) 0.43 mAh cm$^{-2}$ stripped, (iii) 0.95 mAh cm$^{-2}$ stripped, (iv) 0 mAh cm$^{-2}$ plated (equivalent to 1 mAh cm$^{-2}$ stripped), (v) 0.5 mAh cm$^{-2}$ plated, and (vi) 1.1 mAh cm$^{-2}$ plated. The electrochemical cycling profile is shown in Fig. S10. In the grayscale profiles, the SSE interface is indicated by red lines. The nearest Na domain (high grayscale intensity) to the interface is shown with a green line, and other Na domains are marked by blue lines. The white box in (a) marks the location of these cross-sectional images. (c-e) Simulated stripping analysis to determine the evolution of Li and Na coverage at the SSE interface. (c) Rendered 3D subvolumes in the pristine state (top) and after simulated Li stripping (bottom), where Li is gray and Na is white. The reconstructed initial volume measures 420 × 420 × 131 μm$^3$. The accumulation of Na at the SSE interface was simulated by removing Li voxels from the initial state to a thickness of 14 μm (10 voxel layers), while Na remained (Fig. S12 and methods contain details). (d) Interfacial coverage of Na and Li in the subvolume during the first (top panel) and second (bottom panel) stripping processes via simulated Li stripping. (e) 2D interfacial coverage maps at different simulated stripping states, as marked in (d). Li is gray and Na is white.
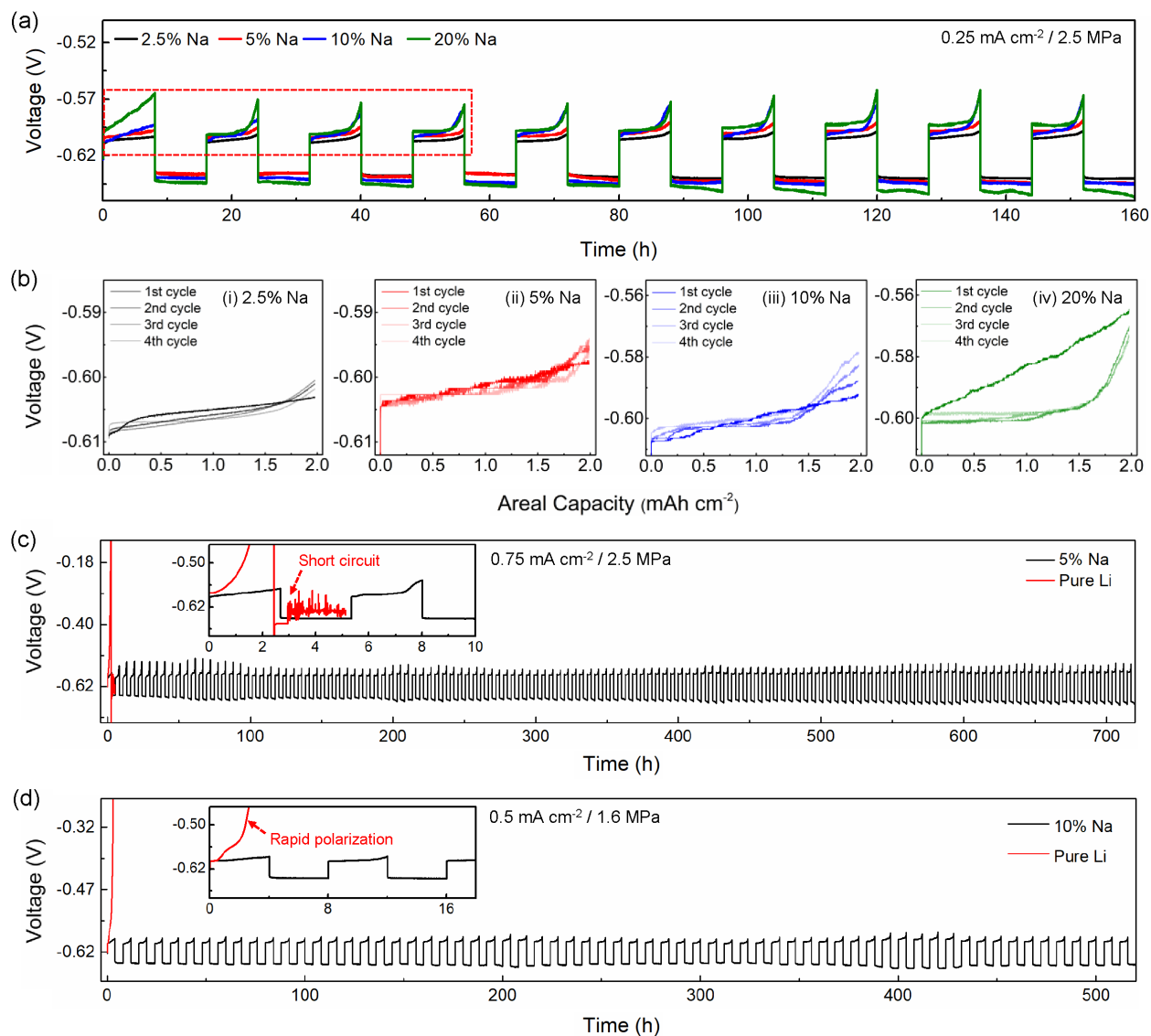
**Figure 4. Galvanostatic cycling tests of Li/Na electrodes.** (a) Cycling of various electrodes with different compositions (2.5-20 at.% Na) at a current density of 0.25 mA cm$^{-2}$ and a stack pressure of 2.5 MPa. (b) Corresponding stripping voltage profiles for the first four cycles, as highlighted within the red box in (a). (c, d) Long-term cycling stability of (c) 5% Na and (d) 10% Na electrodes. For comparison, pure Li electrodes were cycled under the same conditions as in (c) and (d). The cells in (c) were cycled at a current density of 0.75 mA cm$^{-2}$ and a stack pressure of 2.5 MPa, while those in (d) were cycled at a current density of 0.5 mA cm$^{-2}$ and a stack pressure of 1.6 MPa. All cells utilized a LiIn counter electrode and were tested with an areal capacity of 2 mAh cm$^{-2}$ per cycle.
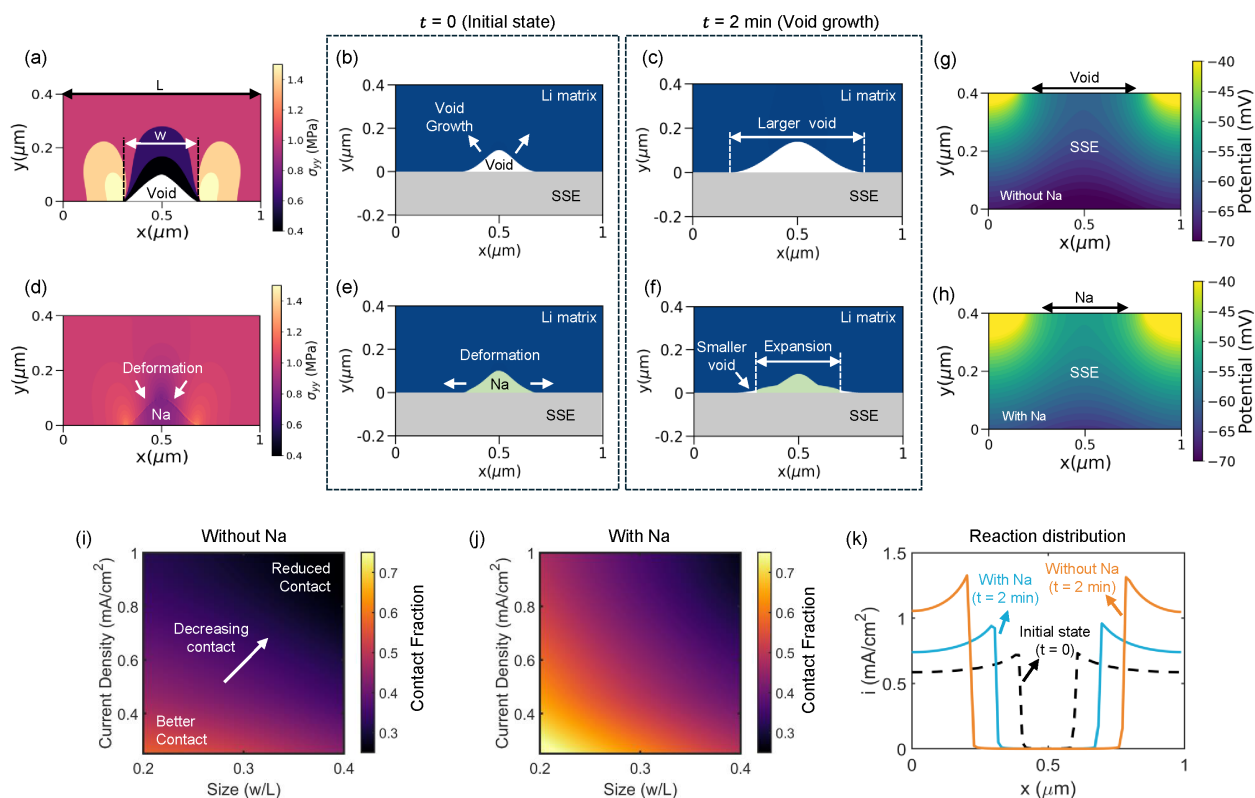
18

**Figure 5. Electro-chemo-mechanical modeling of the evolution of the SSE interface.** (a) Normal stress along y-direction in Li metal with a void at the SSE interface. The void size $w/L$ = 0.3 ($w$ is the void width and $L$ is the model dimension). (b, c) Li-SSE interfacial evolution and void growth from time (b) $t$ = 0 to (c) $t$ = 2 min with an applied current density ($I_{App}$) of 0.5 mA cm$^{-2}$. (d) Normal stress along y-direction in Li metal with Na at the SSE interface (Na size $w/L$ = 0.3). The other stress components are included in Fig. S17. (e, f) Li-SSE interfacial evolution from time (e) $t$ = 0 to (f) $t$ = 2 min when Na is present at the interface ($I_{App}$ = 0.5 mA cm$^{-2}$). (g, h) Electric potential distribution in the SSE with (g) void and (h) Na at the Li-SSE interface. (i, j) Effects of current density and void/Na size on Li-SSE contact fraction with (i) void and (j) Na domain. (k) Reaction current density at the Li-SSE interface with and without Na at time $t$ = 0 and $t$ = 2 min. $I_{App}$ is 0.5 mA cm$^{-2}$, and the void or Na domain size ($w/L$) is 0.2. The stack pressure applied in this model is 1 MPa. The mathematical formulation utilized for this model is described in the SI.